Nanotechnology

Novel Phosphorus Based 2D Allotropes with Ultra High Mobility

To cite this article before publication: Sumandeep Kaur *et al* 2020 *Nanotechnology* in press https://doi.org/10.1088/1361-6528/ab8cf1

Novel Phosphorus Based 2D Allotropes with Ultra High Mobility

Sumandeep Kaur[1, 4*], Ashok Kumar[2*], Sunita Srivastava[1,3], K. Tankeshwar[1, 3] and Ravindra Pandey[4]

[1]*Department of Physics, Panjab University, Chandigarh 160014, India*
[2]*Department of Physics, School of Basic and Applied Sciences, Central University of Punjab, Bathinda, 151001, India*
[3]*Department of Physics, Guru Jambheshwar University of Science and Technology, Hisar, 125001, Haryana, India*
[4]*Department of Physics, Michigan Technological University, Houghton, MI, 49931, USA*

(March 27, 2020)

*Email: Ashok Kumar (ashokphy@cup.edu.in)
Sumandeep Kaur (dusuman0015@gmail.com)

Abstract

Electronic structure calculations based on density functional theory were performed to investigate structural, mechanical and electronic properties of the phosphorene-based large honeycomb dumbbell (LHD) hybrid structures and a new phosphorene allotrope, referred to as ψ"-P. The LHD hybrids (i.e. X_6P_4; X being C/Si/Ge/Sn) and ψ"-P have significantly higher bandgaps than the corresponding pristine LHD structures except the case of C_6P_4, which is metallic. ψ"-P is found to be highly flexible p-type material which shows strain-engineered photocatalytic activity in a highly alkaline medium. Moreover, the carrier mobility of the considered systems comes out to be as high as 10^5 $cm^2V^{-1}s^{-1}$ (Specifically the electron mobility of LHD structures). The calculated STM images display the surface morphologies of LHD hybrids and ψ"-P. It is expected that the predicted phosphorus-based 2D structures with novel electronic properties can be candidate materials for nanoscale devices.

Keywords: Density Functional Theory, Phosphorene, Silicene, Carrier mobility, STM

1 Introduction

Monolayers of group-IV elements i.e., graphene [1,2], silicene [3,4], germanene [5,6] and stanene [7,8] can exist in the honeycomb structure with graphene only being planar. Silicene, germanene, and stanene prefer buckled structures in their ground state configurations preserving Dirac cone-like characters at the Fermi level. An absence of the bandgap, therefore, hinders the use of the group-IV elemental monolayers in the device-related applications including the one in which the switching property is essential [9].

The appropriate experimental methods available are still not advanced enough for the large scale production of two dimensional materials[10,11]. Therefore the experimental synthesis of the 2D materials is slow. However due to the advancement of computational technology there are various computational methods available (e.g. Density Functional Theory) that can be used to predict various materials and their properties.

In recent years, stability of several allotropes of the group-IV elemental monolayers was predicted including MoS_2-like, graphene-like (HEX), trigonal dumbbell (TD), honeycomb dumbbell (HD) and large honeycomb dumbbell (LHD) configurations. It has been reported that the group-IV elemental monolayers except carbon energetically prefer the dumbbell configurations over the all other allotropic configurations, e.g. silicene and germenene are predicted to prefer LHD configuration as their ground state structures [12,13]. Note that sp^2- and sp^3- hybridized atoms constitute the LHD configuration. An unit cell of LHD configuration consists of 10 atoms, out of which four atoms are three-fold coordinated while rest of the atoms are four-fold coordinated [14–16].

A monolayer of black phosphorus (i.e. phosphorene) is of great research interest because of its structural anisotropy, high lateral flexibility, strain engineered electronic properties[17,18] , controlled conduction[19,20], finite band gap, and high carrier mobility up to 10^3 $cm^2V^{-1}s^{-1}$ (experimental) [21,22]. A theoretical study even predicted hole mobility of phosphorene as high as 10^4 $cm^2V^{-1}s^{-1}$ [21]. Its applications include its use in designing various nanoelectronic devices[23], as a sensing device[24] and in spintronics[25,26]. Also, based on ambipolar phosphorene FETs, fully complementary logic inverter has been demonstrated which possess high gain and high noise margin and are chemical doping free[27]. Further for improvement of FET performance, high dielectric material such as HfO_2 can be used which is found to enhance the mobility at room temperature and instead of using solid state back gate, an electric double layer ionic liquid gate shows drastic improvement in the subthreshold swing[28]. Several allotropic configurations of phosphorene including α-, β-, γ-, δ-, red-, ε-, ς-, η-, θ-, octa-, hexstar- and ψ-

Reviewer III

phosphorene have been predicted by the calculations based on density functional theory [29–31], though only α- and β-phosphorene have been synthesised [32,33]. α-P, β-P, γ-P, δ-P and R-P exhibit a buckled honeycomb structure consisting of a six-membered ring similar to graphene, while ε-P, τ-P, η-P, θ-P, ψ--P, O-P, and H-P crystallize into non-honeycomb structural arrangements. Red phosphorene is constructed by the in-plane connections of the segments of α-P and β-P [34]. ε-P and τ-P consist of squared units of phosphorus atoms while η-P and θ-P have phosphorus atoms in the pentagon structural arrangement[35]. ψ-P consists of 4, 6 and 10 membered rings[36], and the octa-P allotrope contains a unique atomic octagonal tiling (OT) pattern consisting of four and eight membered rings[37]. The phosphorus atoms in H-P form a hexagonal lattice with a Magen–David-like top view[38]. Considering that α-P is formed by sp^3 hybridized P atoms in which each P atom is three-fold coordinated with a lone-pair of electrons, the question naturally arises: *Can a dumbbell-like (e.g. LHD) configuration exist for phosphorene?*

In this article, we investigate stability and electronic properties of LHD configuration for phosphorene by employing density functional theory. Calculations are based on initial LHD configurations of the group-IV elemental monolayers in which the group-IV atoms are replaced with P atoms. We show that the resulting phosphorene allotrope is a highly flexible p-type 2D material which consists of 4, 6 and 10 membered rings similar to the ψ-P configuration, though arrangement of the atoms is entirely different [36]. The predicted new phosphorene allotrope is then referred to as ψ''-P in the rest of the paper.

In Sec 2, we provide details of the computational model, and the results are discussed in Sec 3 which is divided into three parts: (i) LHD allotropes of the group-IV elemental monolayers; (ii) the hybrid LHD allotropes – C_6P_4, Si_6P_4, Ge_6P_4, and Sn_6P_4, and (iii) a new phosphorene allotropes - ψ''-P. Finally, Sec 4 summarizes the results.

2 Computational Model

In the calculations based on density functional theory (DFT), the exchange and correlation functional energies were treated using the generalized gradient approximation (GGA) within Perdew-Burke-Ernzerhof (PBE) parameterization[39] as implemented in SIESTA software package[40]. The Kohn-Sham orbitals were expanded as a linear combination of numerical pseudo atomic orbitals using a split-valence double zeta basis set with the polarization functions. The confinement energy of numerical pseudo-atomic orbitals was taken to be 0.01 Ry, and structures were relaxed until the force on each atom was less than 0.01 eV/Å. The Monkhorst-Pack scheme was used to sample Brillouin zone with a (30×30×1) mesh for all

the structures considered. The spacing of the real space used to calculate the Hartree, exchange and correlation contribution of the total energy and Hamiltonian was 450 Ry. A vacuum region of about 20 Å perpendicular to 2D plane was used to prevent the superficial interactions between the periodic images in calculations. For Sn based systems relativistic pseudopotential has been used for correct description of its properties.

The cohesive energy was calculated using the formula:

$$E_C = \frac{E_T - N_{IV}E_{IV} - N_P E_P}{N_T} \quad (1)$$

where E_T is the total energy of the system, E_{IV} (E_P) is the energy of single C/Si/Ge/Sn (P) atom, N_T is the total number of atoms, and N_{IV} (N_P) is the number of C/Si/Ge/Sn (P) atoms in a given configuration.

The room-temperature electron and hole mobilities were calculated by applying a phonon-limited scattering model including the anisotropic characteristics of effective mass, elastic modulus and deformation potential using the formula [41]:

$$\mu_{2D} = \frac{e\hbar^3 C_{2D}}{K_B T m^* m_a^* E_i^2}, \quad (2)$$

where, e is the electronic charge, $\hbar$ is the reduced Plank's constant, T is the temperature, k_B is the Boltzmann constant, m^* is the effective mass in either along *x*- or *y*- direction, m_a^* is the average effective mass given by $\sqrt{m_x^* m_y^*}$. E_i is the deformation potential constant calculated using the formula $E_i = \frac{dE_{edge}}{de}$ where E_{edge} is the energy of the CBM (VBM) for electrons (holes) and $e = \Delta l/l_0$. In-plane elastic modulus is calculated using: $(E - E_0)/S_0 = C_{2D}\,(\Delta\, l/l_0)^2/2$, where E-E_0 represents total energy change, S_0 is the area of the 2D cell and $\Delta l/l_0$ is the strain along x or y direction [42]. Note that to obtain the accurate values of the carrier mobilities is quite challenging and the above formula does not take into account the scattering processes and hence gives only a rough estimate of the carrier mobilities [43].

The BTH formalism with STM-like setup was used to study tunnelling characteristics of given structures, where electron tunnelling current is calculated as follows:

$$I = \frac{4\pi e}{\hbar}\int_{-\infty}^{+\infty} \rho_s\left(\varepsilon + \frac{eV}{2}\right)\rho_t\left(\varepsilon - \frac{eV}{2}\right) e^{-2d\left(2\left(\frac{m}{\hbar^2}\right)(\varphi_{av} - \varepsilon)\right)^{\frac{1}{2}}} \left\{\left[f\left(\varepsilon - \frac{eV}{2}\right)\right]\left[1 - \left[f\left(\varepsilon + \frac{eV}{2}\right)\right]\right] - \left[f\left(\varepsilon + \frac{eV}{2}\right)\right]\left[1 - \left[f\left(\varepsilon - \frac{eV}{2}\right)\right]\right]\right\} d\varepsilon \quad (3)$$

where e is the electronic charge, m is the effective mass of the electron, $\hbar$ is the Planck constant, ρ_s and ρ_t represents the projected densities of states (PDOS) of the sample (monolayers) and the tip (Au_{13} cluster), respectively; ε is the injection energy of the tunnelling electron, d is the

distance between tip and sample, φ_{av} is the average work-function of the sample and the tip and f is the Fermi distribution function. The tip was considered to be separated from the sample by a vacuum barrier width of 5 Å, which depicts a non-bonded tip configuration for the STM calculations.

Note that PDOS and the HSE bandgap were obtained from VASP-DFT calculations[44]. In the hybrid Heyd-Scuseria-Ernzerhof HSE06 method, the exchange-correlation functional uses a mixing parameter to incorporate Hartree-Fock (HF) exact exchange functional and the PBE functional.

3 Results and Discussion

To test the reliability and accuracy of the modelling elements, we first consider the LHD (Large Honeycomb Dumbbell) structures of the group-IV elemental monolayers (as shown in figure 1(a) where the top view consists of two type of six membered rings while the side view looks like chain of dumbbells), and compare the results of our calculations with the previously reported results [12]. Since no information about mechanical property or electronic mobilities are available in the scientific literature, we provide the corresponding results, for the first time, for the LHD structures of the group-IV elemental monolayers.

Next, we consider the hybrid LHD configurations, X_6P_4 with X being C, Si, Ge and Sn in which only sp^3 sites were occupied by P atoms in the 2D lattice. Note that sp^3 sites are uppermost and lowermost atoms in the side view of figure 1(a). The results discussing stability, mechanical and electronic properties of the hybrid LHD configurations are presented. Finally, we report, for the first time, a new phosphorene allotrope, ψ''-P which is found to be stable with *p*-type electronic properties.

3.1 Group-IV elemental monolayers: dumbbell configurations

3.1.1 Stability:

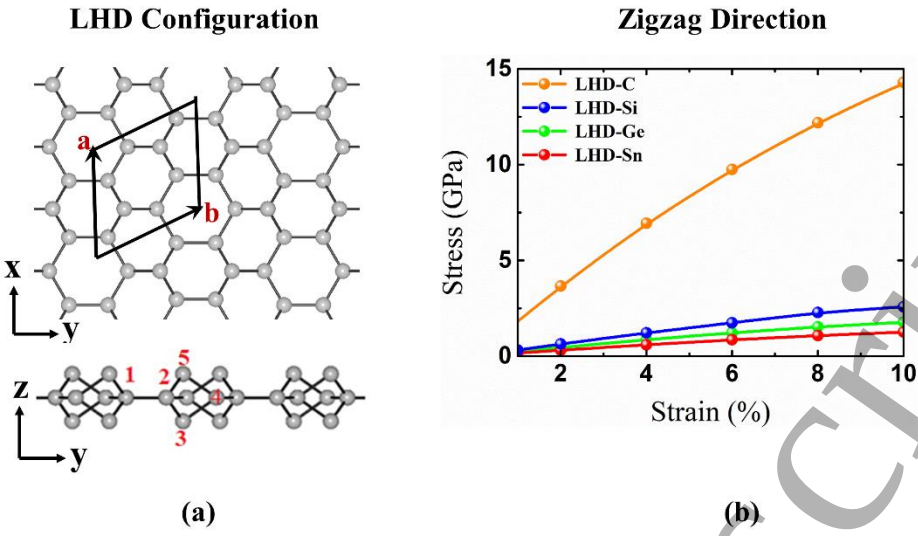

Figure 1: (a) Top and side views of the crystal structure and (b) stress-strain curve along the zigzag direction of group IV elements in LHD configuration.

Figure 1 displays top and side views of a LHD configuration consisting of two types of six-membered rings in the 2D lattice. The calculated lattice constants associated with LHD-C, LHD-Si, LHD-Ge and LHD-Sn are found to be in good agreement with the previously reported values (Table S1, Supplementary Information) [12]. The buckling height (*d*) (i.e. distance between atom 5 and atom 3 in Figure 1) is consistent with previously reported DFT values (Table S1, Supplementary Information) [12].

To check the mechanical stability of LHD configurations of the group-IV elemental monolayers, calculations were performed to obtain the stress-strain relationship. Note that the stress-strain relation can estimate the ultimate tensile strength of a material which can be defined as the ultimate value of stress (UTSR) at ultimate value of strain (UTSN) where the slope of stress-strain curve becomes zero. This will give us the maximum value of strain and stress that a material can withstand before breaking (Figures 1(b) and S1 (a) of Supplementary Information). For LHD-C, the calculated (UTSR, UTSN) is (19 GPa, 20%) along zigzag and (17 GPa, 16%) along armchair directions. In case of LHD-Si, (UTSR, UTSN) is (3.2 GPa, 20%) along zigzag direction and (3 GPa, 16%) along the armchair direction. For LHD-Ge, (UTSR, UTSN) is (2.2 GPa, 20%) along zigzag, and (2 GPa, 16%) along armchair directions. For LHD-Sn, (UTSR, UTSN) is (1.7 GPa, 20%) along zigzag and (1.6 GPa, 16%) along armchair directions.

Also, the mechanical flexibility of a 2D configuration can be interpreted in terms of the in-plane elastic modulus (C_{2D}) in the propagation direction. The in-plane stiffness is found to be isotropic with magnitude 336 N/m, 77.8 N/m, 57.4 N/m and 39.7 N/m respectively for LHD-C, LHD-Si, LHD-Ge and LHD-Sn, following the trend LHD-C > LHD-Si > LHD-Ge > LHD-

Sn. The experimental value of elastic modulus of graphene is found to be 340 N/m which is comparable to our calculated value for LHD-C [45]. This trend can be understood in terms of the bond lengths; a smaller bond length representing a stronger bond corresponds to a larger in-plane stiffness. The (average) bond lengths in these structures follow the trend of C-C< Si-Si< Ge-Ge< Sn-Sn. The high in-plane-stiffness in case of LHD-C can be understood from the relatively high induced stress in LHD-C structure on application of strain compared to other group-IV dumbbell configurations which makes it least flexible of all the LHD structures (Figure 1(b)).

3.1.2 Electronic Properties:

The GGA band gaps of LHD configurations of the group-IV elements are calculated to be 1.8 eV for LHD-C, 0.3 eV for LHD-Si, 0.02 eV for LHD-Ge and 0.1 eV for LHD-Sn. These values are consistent with the scientific literature [12] following the trend of LHD-C > LHD-Si > LHD-Sn > LHD-Ge. Since the DFT is known to underestimate the bandgap at the GGA level of theory, we calculate the bandgaps using HSE06 hybrid functional as well[17]. A comparison of the GGA and HSE06 bandgaps clearly depicts this underestimation. The HSE06 hybrid functional band gaps of these configurations are calculated to be 2.69 eV for LHD-C, 0.77 eV for LHD-Si, 0.37 eV for LHD-Ge and 0.33 eV for LHD-Sn. The major contribution to the bands near the Fermi level comes from the 2p, 3p, 4p and 5p orbitals of C-, Si- Ge- and Sn-atoms in LHD-C, LHD-Si, LHD-Ge and LHD-Sn, respectively (Figure S2, Supplementary Information).

Table 1. Calculated electron and hole effective mass (m^*), deformation potential (E_1), carrier mobilities (μ) and mobility anisotropy (R_a) of LHD-C, LHD-Si, LHD-Ge and LHD-Sn along the zigzag and armchair directions.

	Effective mass		***Deformation potential***		***Mobility***		***Mobility anisotropy***
Systems	m^* **(x)** (m_e)	m^* **(y)** (m_e)	E_{1x} **(eV)**	E_{1y} **(eV)**	μ **(x)** ($cm^2/V/s$)	μ **(y)** ($cm^2/V/s$)	R_a
LHD-C (e)	1.71	1.66	0.31	0.30	2.6×10^4	2.9×10^4	1.10
LHD-C (h)	0.18	0.17	3.44	3.45	1.9×10^4	2.1×10^4	1.11
LHD-Si (*e*)	0.37	0.37	0.88	0.86	4.3×10^4	1.7×10^4	2.58
LHD-Si (*h*)	0.67	0.12	2.60	2.59	1.3×10^3	7.0×10^3	5.44
LHD-Ge (*e*)	0.33	0.33	0.34	0.41	9.8×10^4	6.6×10^4	1.48
LHD-Ge (*h*)	0.62	1.0	1.98	2.0	6.5×10^3	3.9×10^2	1.65
LHD-Sn(*e*)	0.37	0.37	0.29	0.32	7.4×10^4	5.9×10^4	1.27
LHD-Sn(*h*)	0.87	0.44	1.48	1.49	7.20×10^2	1.4×10^3	1.97

The electronic properties of the material are greatly influenced by the mobility of the carriers in that material. The carrier transport properties depend on the in-plane stiffness, carrier effective mass and deformation potential. The carrier effective mass can be calculated by quadratic fitting of the band near the conduction band minima (CBM) or valence band maxima (VBM). A smaller value of the carrier effective mass leads to increase in the carrier mobility. To check the amount of anisotropy in the carrier mobility, the mobility anisotropy is calculated using: $R_a = \frac{Max(\mu_x,\mu_y)}{Min(\mu_x,\mu_y)}$, where R_a = 1 for isotropic systems and R_a>1 for anisotropic systems [46].

Table 1 lists magnitude of carrier effective mass, deformation potential and carrier mobility obtained using Eq. 2, of the considered systems. For LHD-C, the electron and hole effective masses are nearly isotropic whereas only the electron effective mass is found to be isotropic for LHD-Si, LHD-Ge and LHD–Sn.

The calculated results suggest dumbbell configurations of the group-IV elemental monolayers to be *n*-type semiconductors with very high electron mobilities of the order 10^4 $cm^2/V/s$ [Table 1].

The surface morphology of a material can be investigated using STM images. First principles calculations have been well known to simulate the STM images by applying a small bias voltage V_{bias} between the STM tip and the sample which yields a tunnelling current with density j(r) proportional to the local density of states (LDOS) at the centre of the curvature of the tip at (r), approximated by Tersoff and Hamann expression [47]. LDOS is integrated from (E_F–eV) to E_F (Fermi energy). The s-waves with constant density of states describe the tip states. A positive (negative) bias voltage indicates tunnelling from the occupied states of the sample to the tip (tip to unoccupied states of the sample) [48–51].

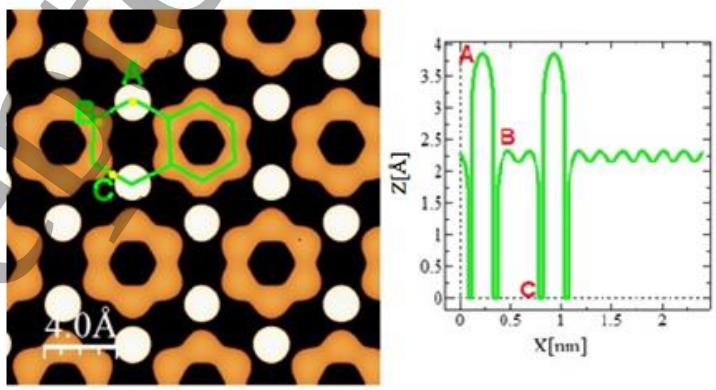

Figure 2: The STM images and distance versus height profile for LHD-Si. The size of STM images is 20Å × 20Å with an iso-surface value of 0.001 eV/Å and the bias voltage is 1.0 V.

In the STM image, brightest colours indicate atoms on top and dark colours indicate atom located in bottom in the buckled 2D lattice. A comparison of the top view of the crystal structure with that of the STM image shows that the STM images can clearly guide the experimentalists to predict the surface of these considered LHD systems (Figures 2 and S3 of Supplementary Information). Three different heights represented by A and B depicted in the distance-height profile of LHD-Si corresponds to the atom at position 5 and position 2 as given in Figure 1(a), while C corresponds to no atom. No STM image is obtained for LHD-C since the bias voltage of 1.0 V is far less than its bandgap of about 1.86 eV.

Tunnelling characteristics calculated within BTH formulation (Eq 3) find LHD-Ge, and LHD-Sn configurations exhibiting nearly-Ohmic character (≈very small band-gaps), though LHD-Si exhibits diode-like characteristics (≈a noticeable finite gap (Figures 3).

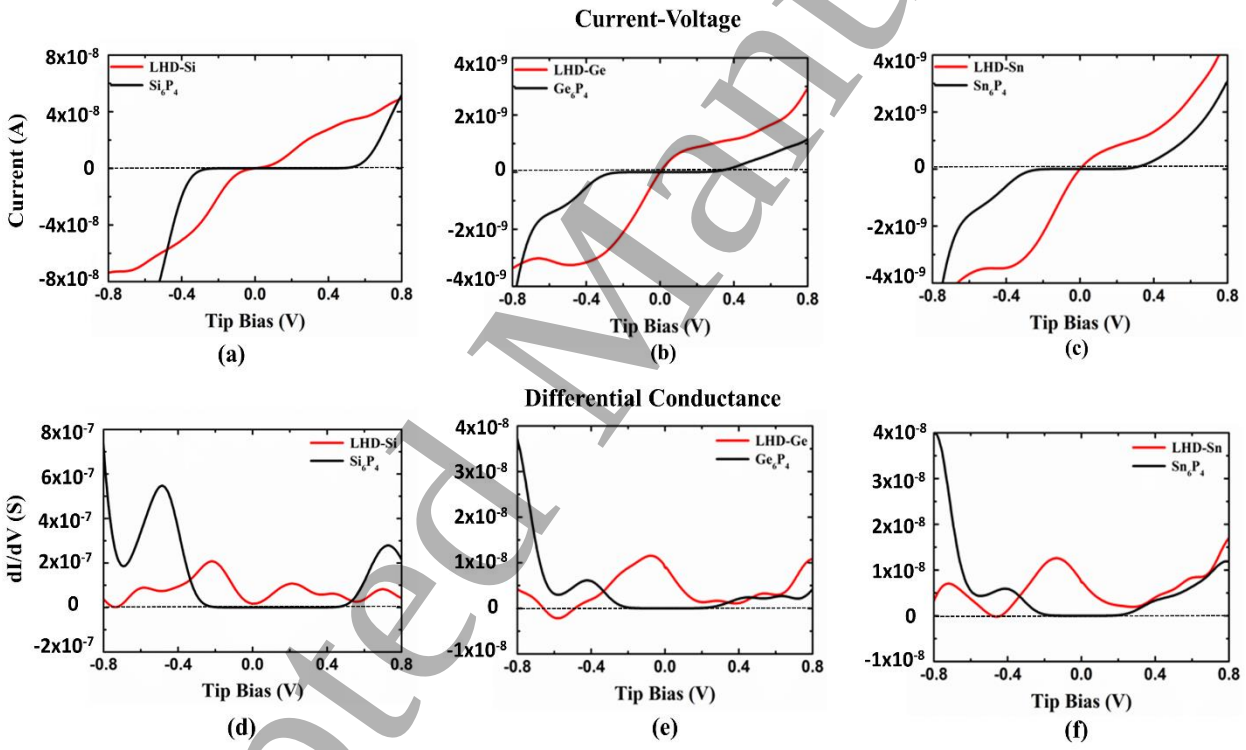

Figure 3: The current-voltage characteristics and differential conductance of LHD-Si, Ge and Sn and the hybrid Si_6P_4, Ge_6P_4 and Sn_6P_4

3.2 Hybrid LHD Structures: C_6P_4, Si_6P_4, Ge_6P_4 and Sn_6P_4

3.2.1 Stability:

The hybridized structures were formed by replacing completely the sp^3-coordinated atoms of LHD structure with P atoms (Figure 4(a)). Recall that a LHD configuration consists four atoms with sp^3 hybridization in the 2D lattice, and sp^3 hybridization is found to be favoured by P-atoms as can be seen in its 2D allotropes [29-42]. Note that the calculated results find that an

incremental addition of P atoms at sp^3 sites increases the cohesive energy except in LHD-C where it decreases almost continuously (Figure S4, Supplementary Information). Once all the sp^3 sites are occupied by P atoms, further addition of P-atoms at any of the sp^2 site destroys dumbbell-like configurations.

The hybrid X_6P_4 (X: C/Si/Ge/Sn) structures shown in Figure 4(a) are predicted to be dynamically stable. As a representative case, we present the phonon spectra of Si_6P_4 in Figure S5 of Supplementary Information. Note that the X-P bond length (X3-X4 in Figure 4(a)) is less than the X-X bond length (X1-X2), except for C_6P_4 (Table S1, Supplementary Information) in which the C-C bond length (1.53 Å) is less than the C-P bond length (1.94 Å). The calculated buckling heights (*d*) for the hybrid LHD configurations are 2.55 Å (C_6P_4), 3.37 Å (Si_6P_4), 3.44 Å (Ge_6P_4) and 3.69 Å (Sn_6P_4), respectively (Table S1, Supplementary Information).

Figures 5 and S1 (b) of Supplementary Information depicts the stress-strain relationship for the hybrid X_6P_4 configurations. The values of ultimate tensile strain/strength (UTSR/UTSN) for C_6P_4 is (10.4GPa, 16%) along zigzag and (11.1GPa, 16%) along armchair directions. For Si_6P_4 (UTSR/UTSN) is (3.1GPa/ 18%) along zigzag and (3.2GPa/ 16%) along armchair directions. For Ge_6P_4, (UTSR, UTSN) is (1.85GPa, 12%) along zigzag and (1.88GPa, 18%) along armchair directions, and for Sn_6P_4, (UTSR, UTSN) is (1.38GPa, 14%) along zigzag and (1.37GPa, 12%) along armchair directions. The in-plane stiffness is found to be 76.1 N/m, 61.5 N/m and 44.2 N/m for Si_6P_4, Ge_6P_4 and Sn_6P_4 which follows the trend $Si_6P_4 > Ge_6P_4 > Sn_6P_4$.

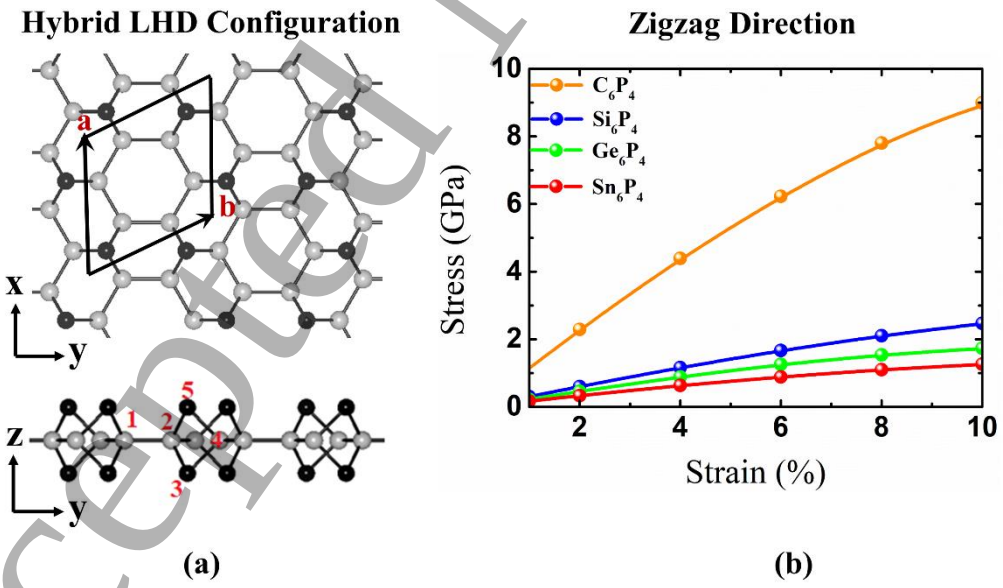

Figure 4: (a) Top and side views of the crystal structure and (b) stress-strain curve along the zigzag direction of group-IV elements in hybrid LHD configuration. Grey coloured balls represent group-IV atoms (C/Si/Ge/Sn) while black coloured balls indicate P-atoms.

3.2.2 Electronic Properties:

The addition of a P atom increases the bandgap exception being LHD-C. In the case of LHD-C, the bandgap is 1.83 eV which reduces to 0 eV for C_6P_4, exhibiting a semiconductor to metal transition (Figure 5). The GGA (HSE06) bandgaps of Si_6P_4, Ge_6P_4 and Sn_6P_4 are calculated to be 1.24eV (1.69eV), 0.94eV (1.23eV) and 0.63eV (1.09eV), respectively, which is significantly higher than their LHD counterparts. The predicted difference in C_6P_4 vs. others hybrid LHD structures may likely to be due to the greater electronegativity of both C and P that results into a strong C-P bond leading to the localized states at the Fermi level of C_6P_4.

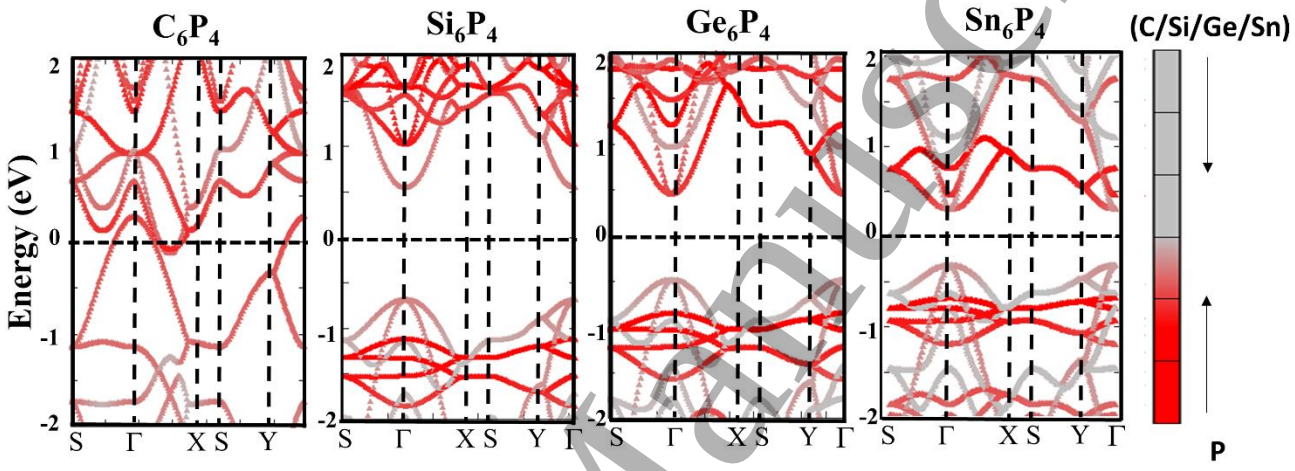

Figure 5: Band-structure of the hybrid LHD configurations.

Table 2. Calculated electron and hole effective mass (m^*), deformation potential (E_1), carrier mobilities (μ) and mobility anisotropy (R_a) for Si_6P_4, $Ge_6P_4$and Sn_6P_4 along the zigzag and armchair directions.

	Effective mass		*Deformation potential*		*Mobility*		*Mobility anisotropy*
Systems	m^* (x) (m_e)	m^* (y) (m_e)	E_{1x} (eV)	E_{1y} (eV)	μ (x) ($cm^2/V/s$)	μ (y) ($cm^2/V/s$)	R_a
Si_6P_4 (*e*)	0.45	0.45	0.31	0.24	$8.6x10^4$	$1.4 x10^5$	1.6
Si_6P_4 (*h*)	1.49	0.26	2.06	1.87	$4.1 x10^2$	$2.9 x10^3$	7.1
Ge_6P_4 (*e*)	0.34	0.08	5.91	6.15	$7.1 x10^2$	$2.9 x10^3$	4.1
Ge_6P_4 (*h*)	1.72	0.15	1.88	1.45	$4.3 x10^2$	$8.3 x10^3$	19.6
Sn_6P_4 (*e*)	0.47	0.07	5.51	3.75	$3.6 x10^2$	$4.9 x10^3$	13.7
Sn_6P_4 (*h*)	1.87	0.13	1.41	0.98	$5.3 x10^2$	$1.6 x10^4$	30.7

In hybrid LHD configurations, CBM remains at the Γ, while VBM moves from a point between Γ and X in the case of pristine LHD configurations to Γ in the case of the hybrid LHD configuration. This shift changes the bandgap character from indirect to direct as the hybrids are formed. CBM in the hybrid monolayers is mainly due to a contribution of the p orbitals of Si/Ge/Sn while the major contribution to VBM is from the P-p orbitals.

The isotropy in the electron effective-mass is retained for Si_6P_4 while the electron effective-mass becomes anisotropic for Ge_6P_4 and Sn_6P_4 (Table 2). The hole effective-mass, on the other hand, remains anisotropic on forming the hybrid LHD structures. In the case of Si_6P_4, the ultra-high electron mobilities were predicted with value of the order of 10^5 which is the highest value reported among all the considered configurations. Such high electron mobilities are of extreme significance in the nano-electronic devices. Ge_6P_4 acts as an *n*-type (*p*-type) material along the zigzag (armchair) direction and Sn_6P_4 possesses *p*-type character along zigzag as well as armchair direction. It is worth calculating the effect of spin orbit coupling (SOC) on the carrier mobility in Sn based system. Electronic bands structure calculated including SOC effect show significant reduction in the band gap of Sn_6P_4 (SOC bandgap of Sn_6P_4: 0.52eV) due to splitting of valance band maximum (Figure S6 Supplementary Information), however, the carrier mobility does not change to a larger extent (Table S2 of Supplementary Information). The fitted curves for in-plane stiffness and deformation potential for Sn_6P_4 as a representative case has been shown in Figure S7.

Next, the STM images depict three different regions labelled as A, B and C corresponding to different heights of atoms in the hybrid lattice (Figure 6). The calculated tunnelling characteristics find the diode-like characteristics for the hybrid structures unlike the Ohmic characteristics shown by the pristine LHD structures (Figure 3).

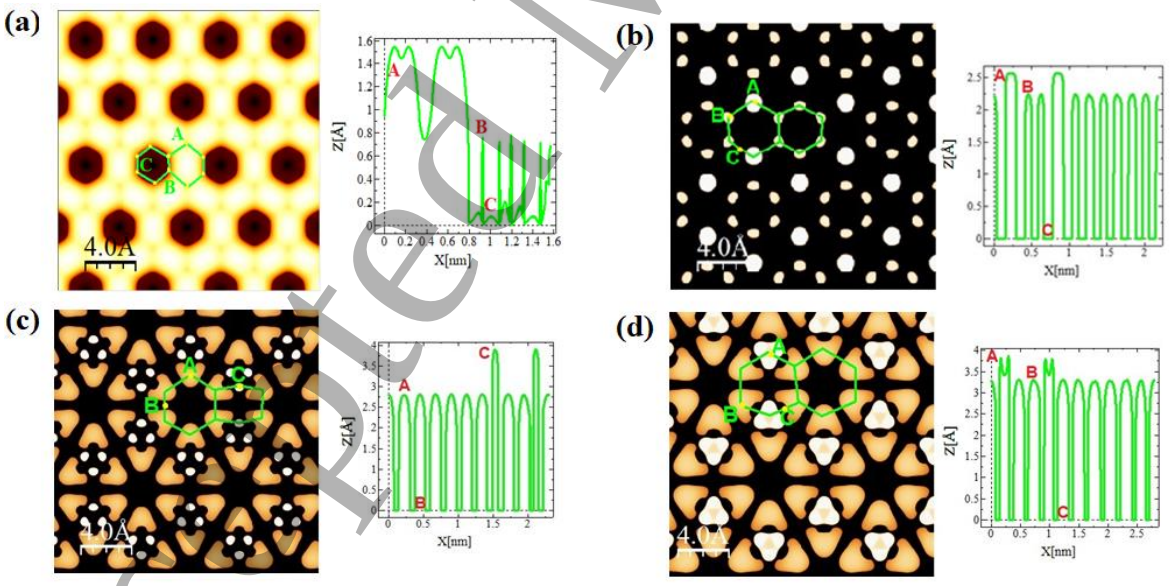

Figure 6: The STM images and distance versus height profile for (a) C_6P_4, (b) Si_6P_4, (c) Ge_6P_4 and (d) Sn_6P_4. The size of STM images is 20Å × 20Å with an iso-surface value of 0.001 eV/Å and the bias voltage is 1.0V.

3.3 New P allotrope, ψ''-P

3.3.1 Stability:

We now address the question of "*does a dumbbell-structure exist for phosphorene*?" by replacing the sp^2 sites with P-atoms in the hybrid X_4P_6 configurations. The calculated results find that replacing all C/Si/Ge/Sn atoms with P atoms in LHD configuration gives rise to a new 2D phosphorene allotrope (Figure 7 (a)) which is not yet reported in the scientific literature. We replace each atom of the LHD structure one by one with P atom beginning with sp^3 sites and after that the rest of the sites. The structure evolution is shown in Figure S8, Supplementary Information. The calculated cohesive energy of this new phosphorene allotrope is 5.52 eV/atom which is about 0.16 eV/atom lower than α-P (Figure S4, Supplementary Information). This new phosphorene allotrope consists of 4, 6 and 10 membered rings similar to ψ-P, with entirely different atomic arrangements yielding P-P bond lengths of 2.22Å, 2.29Å and 2.32Å (Figure S9 of Supplementary Information) in the 2D lattice. The new allotrope is now referred to as ψ"-P.

The phonon spectra of ψ"-P depicts its dynamical stability (Figure S5, Supplementary Information). The phonon spectra presents little imaginary frequency near gamma point which are probably due to softening of phonons and strongly depend on the computational parameters as pointed out in previous literature[52–54]. The stress-strain relationship shows ψ"-P to be anisotropic. The calculated values of ultimate tensile strain/strength (UTSR/UTSN) is (2.6GPa/ 18%) along zigzag and (18GPa/ 26%) along armchair directions (Figure 7(b)). The anisotropy can also be seen in the values of in-plane stiffness. Compared to α-P, it is found that ψ"-P is flexible along both zigzag and armchair directions with in-plane stiffness value of 72.6 N/m and 26.8 N/m respectively. For α-P, the calculated values of C(x) and C(y) are 105 N/m and 26.5 N/m, respectively.

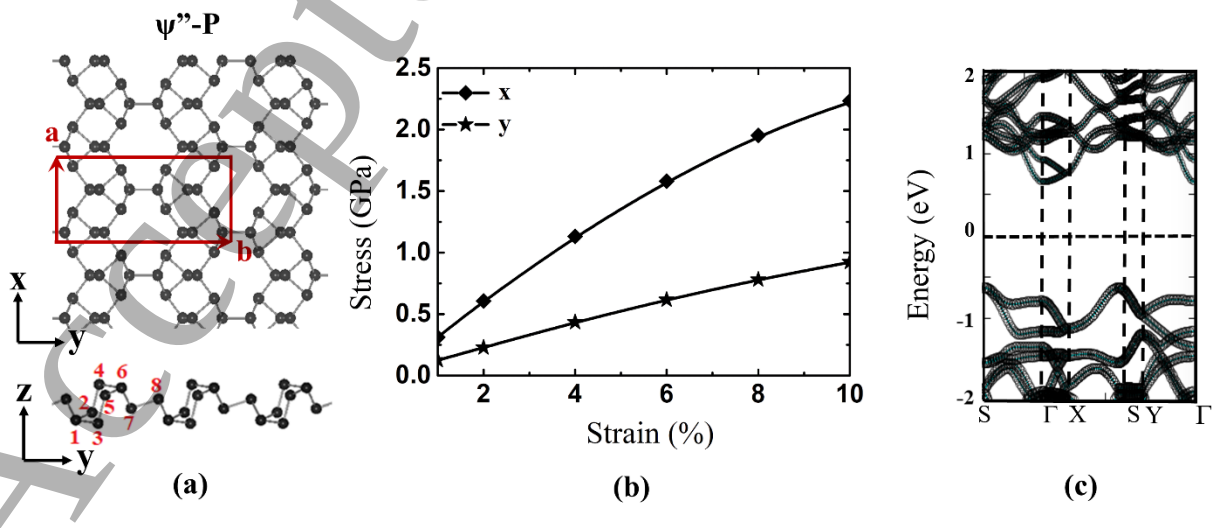

Figure 7: (a) Top and side views of the unit cell, (b) stress-strain curve and (c) band structure of ψ”-P.

3.3.2 Electronic Properties:

The bandgap of ψ”-P is calculated to be indirect with a value of 1.28 eV, and CBM lies at Γ while VBM lies at S point of the Brillouin zone of ψ”-P [Figure 7(c)]. The band gap value calculated using HSE06 hybrid functional is 1.98 eV. We find that both the electron and hole effective-masses are anisotropic; the hole effective-mass is about 10 times higher than the electron effective mass along zigzag direction for ψ”-P. Along the armchair direction, the electron effective-mass is 5 times higher than the hole effective mass for ψ”-P.

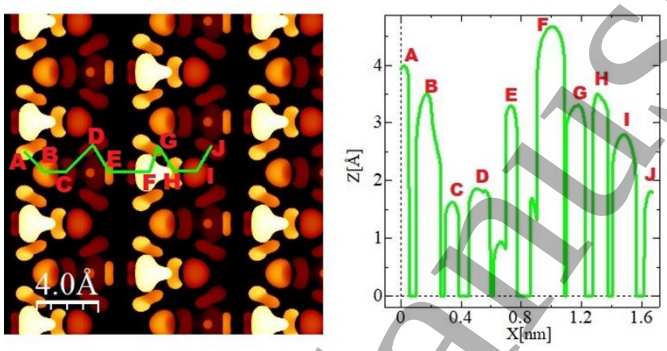

Figure 8: The STM images and distance versus height profile for ψ”-P. The size of STM images is 20Å × 20Å with an iso-surface value of 0.001 eV/Å and the bias voltage is 1.0V.

The STM image of ψ”-P depicts different regions due to the various heights of the atoms (see corresponding distance-height profile Figure 8) as can be seen from the side view of the crystal structure in Figure 7(a). Also, similar to the hybrid LHD structures, ψ”-P show diode like characteristics as depicted in its current-voltage characteristic and differential conductance (Figure 9).

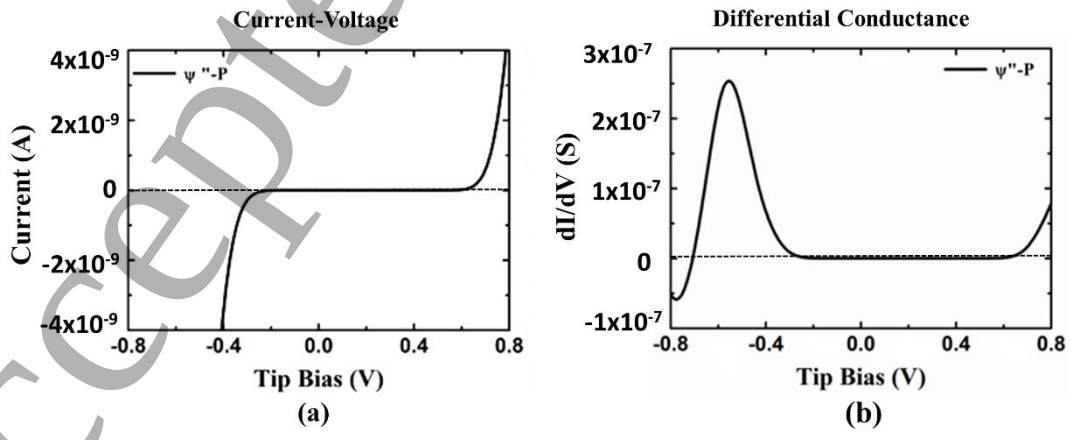

Figure 9: (a) The current-voltage characteristics and (b) differential conductance of the ψ”-P.

The calculated results of the carrier mobility predict ψ"-P to be p-type semiconducting 2D material [Table 3]. The benchmark calculation was performed for α-P for which we find that the calculated effective mass is in good agreement with that reported in the literature [42]. Additionally, we find that the hole mobility is higher than its electron mobility along zigzag (i.e. x) direction. On the other hand, the electron mobility is higher than the hole mobility along armchair (i.e. y) direction. This behaviour then suggests *p* (*n*)-type characteristics along zigzag (armchair) direction for α-P as also previously reported [Table 3] [42].

Table 3. Calculated electron and hole effective mass (m^*), deformation potential (E_1), carrier mobilities (μ) and mobility anisotropy (R_a) for α-P and ψ"-P along the zigzag and armchair directions.

	Effective mass		***Deformation potential***		***Mobility***		***Mobility anisotropy***
Systems	m^* **(x)** (m_e)	m^* **(y)** (m_e)	E_{1x} **(eV)**	E_{1y} **(eV)**	μ **(x)** ($cm^2/V/s$)	μ **(y)** ($cm^2/V/s$)	R_a
α-P (e)	1.24	0.14	5.66	1.12	1.3×10^2	1.1×10^4	84.5
α-P (h)	5.56	0.14	0.46	3.54	2.2×10^3	1.2×10^3	1.82
ψ"-P (*e*)	0.22	1.53	4.96	3.20	7.4×10^1	6.3×10^1	1.2
ψ"-P (*h*)	2.33	0.34	2.32	4.74	4.4×10^2	8.5×10^2	1.9

3.4 Application

There are few examples in literature where the indirect bandgap semiconductors are found to exhibit excellent photocatalytic activity[55,56]. The separation and diffusion rate of the photoinduced electrons and holes are important indexes for an excellent photocatalyst. In general, if the effective mass of the photogenerated carrier is lighter, the carriers will have more probability of reaching the surface reaction sites within their life-time, thus improving the photocatalytic activity. The electron along x direction while hole along y direction possess relatively lighter effective mass in ψ"-P. The significant difference between the electron and hole effective mass in case of ψ"-P leads to the effective separation of the electron–hole pairs, which may reduce the recombination probability of the photogenerated carriers.

The bandgap of the material should be at least 1.23 eV to show photocatalytic activity in the process of water splitting. Not only does the bandgap have this particular value but also the VBM should be more negative than the redox potential of H_2O/O_2 and the CBM of the system should be more positive than the redox potential of H_2/H^+ (0V vs NHE) [57]. The general process can be:

$$(\psi'' - P)^* \rightarrow h^+ + e^-$$

Oxidation (E vs. NHE = 1.23 eV): $H_2O + 2h^+ \rightarrow 2H^+ + \frac{1}{2}O_2$

Reduction (E vs. NHE = 0 eV): $2H^+ + 2e^- \rightarrow H_2$

Overall process: $H_2O \xrightarrow{(\psi''-P)^*/h\upsilon} H_2 + \frac{1}{2}O_2$

The bandgap of ψ”-P is calculated to be greater than 1.23 eV but the VBM is less negative than the redox potential of H_2O/O_2. It is a well-known fact that the bandgap of the material can be tuned by applying the strain [58].

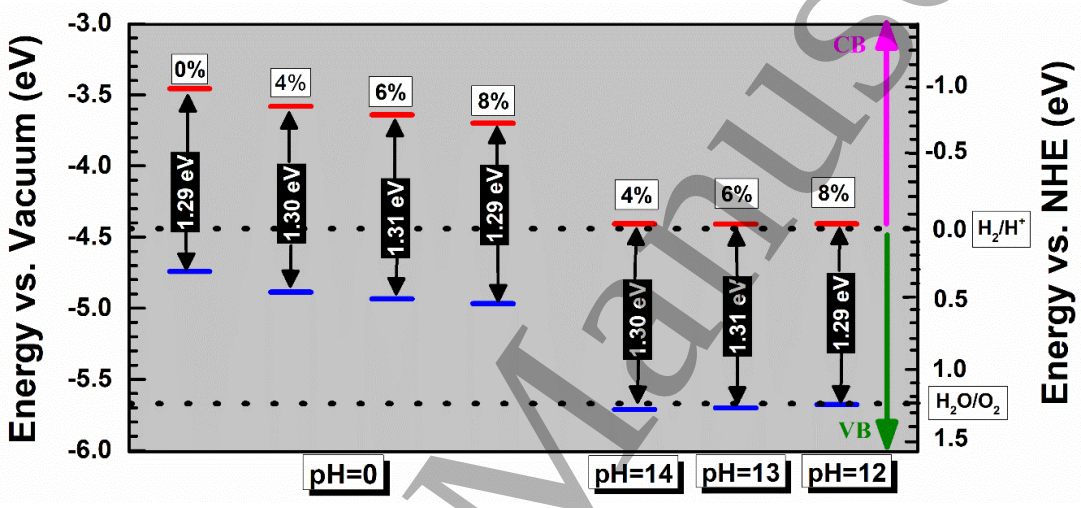

Figure 10: Energy alignment of monolayer ψ”-P allotrope. The strain engineering and pH value of medium can modulate the band alignment. Red (blue) colored horizontal lines indicate CBM (VBM).

Also, the pH value of the solution greatly influences the standard redox potential. In a solution, the standard oxidation potential H_2O/O_2 can be given as [59]:

$$E^{ox}_{O_2/H_2O} = 5.67\ eV - pH \times 0.059\ eV$$

Hence the oxidation and redox potential will shift equally as the pH of the solution changes. So, we found that application of tensile strain of 4 %, 6% and 8 % at pH values of 14, 13 and 12, respectively, makes the band alignments appropriate for its application as a photocatalyst [Figure 10]. Note that, alkaline media provides a less corrosive environment to the catalysts, and the oxidation reduction reaction kinetics is more rapid in alkaline media than in acidic media [60].

4 Conclusion

Based on first principles calculations, a new allotrope of two dimensional phosphorene (ψ"-P) has been predicted along with four phosphorus based novel group-IV LHD hybrids (C_6P_4, Si_6P_4, Ge_6P_4 and Sn_6P_4). The structural phase transition starting from LHD-C/Si/Ge/Sn to C_6P_4/Si_6P_4/Ge_6P_4/Sn_6P_4 to ψ"-P have been discussed. Compared with very low indirect bandgap of the group-IV LHD structures, the predicted hybrids possess direct bandgap with values more than 50% of their corresponding LHD counterparts, exception being the case of carbon based hybrid C_6P_4 which comes out to be metallic. The carrier mobility of these new semiconductors reaches as high as 10^4 to 10^5 $cm^2V^{-1}s^{-1}$. Least value of the carrier mobility is possessed by ψ"-P (~10^3 $cm^2V^{-1}s^{-1}$) but is still higher than most of the 2D materials. The calculated STM images of the considered systems clearly depicts their surface morphology. The new phosphorene allotrope is found to show photocatalytic activity under appropriate solution conditions through strain engineering. The novel electronic properties calculated here makes them suitable candidates for the various nano material based applications.

5 Conflict of Interests

There are no conflicts of interest.

6 Acknowledgement

The RAMA and Superior, High Performance Computing Cluster at Michigan Technological University, Houghton, MI, USA, are used to obtaining the results presented in this paper.

7 References

(1) Matthes, L.; Gori, P.; Pulci, O.; Bechstedt, F. Universal Infrared Absorbance of Two-Dimensional Honeycomb Group-IV Crystals. *Phys. Rev. B* **2013**, *87*, 035438.

(2) Roldán, R.; Chirolli, L.; Prada, E.; Silva-Guillén, J. A.; San-Jose, P.; Guinea, F. Theory of 2D Crystals: Graphene and Beyond. *Chem. Soc. Rev.* **2017**, *46*, 4387.

(3) Zhao, J.; Liu, H.; Yu, Z.; Quhe, R.; Zhou, S.; Wang, Y.; Liu, C. C.; Zhong, H.; Han, N.; Lu, J.; et al. Rise of Silicene: A Competitive 2D Material. *Prog. Mater. Sci.* **2016**, *83*, 24.

(4) Guzmán-Verri, G. G.; Lew, L. C.; Voon, Y. Electronic Structure of Silicon-Based Nanostructures. *Phys. Rev. B* **2007**, *76*, 075131.

(5) Cahangirov, S.; Topsakal, M.; Aktürk, E.; Ciraci, S. Two-and One-Dimensional Honeycomb Structures of Silicon and Germanium. *Phys. Rev. Lett.* **2009**, *102*, 236809.

(6) Bechstedt, F.; Matthes, L.; Gori, P.; Pulci, O. Infrared Absorbance of Silicene and

Germanene. *Appl. Phys. Lett* **2012**, *100*, 261906.

(7) Matthes, L.; Pulci, O.; Bechstedt, F. Massive Dirac Quasiparticles in the Optical Absorbance of Graphene, Silicene, Germanene, and Tinene. *J. Phys. Condens. Matter* **2013**, *25*, 395305.

(8) Xu, Y.; Yan, B.; Zhang, H.-J.; Wang, J.; Xu, G.; Tang, P.; Duan, W.; Zhang, S.-C. Large-Gap Quantum Spin Hall Insulators in Tin Films. *Phys. Rev. Lett.* **2013**, *111*, 136804.

(9) Schwierz, F. Graphene Transistors. *Nat. Nanotechnol.* **2010**, *5*, 487.

(10) Mannix, A. J.; Kiraly, B.; Hersam, M. C.; Guisinger, N. P. Synthesis and Chemistry of Elemental 2D Materials. *Nat. Rev. Chem.* **2017**, *1*, 0014.

(11) Lin, Z.; McCreary, A.; Briggs, N.; Subramanian, S.; Zhang, K.; Sun, Y.; Li, X.; Borys, N. J.; Yuan, H.; Fullerton-Shirey, S. K.; et al. 2D Materials Advances: From Large Scale Synthesis and Controlled Heterostructures to Improved Characterization Techniques, Defects and Applications. *2D Mater.* **2016**, *3*, 042001.

(12) Matusalem, F.; Marques, M.; Teles, L. K.; Bechstedt, F. Stability and Electronic Structure of Two-Dimensional Allotropes of Group-IV Materials. *Phys. Rev. B* **2015**, *92*, 045436.

(13) Ding, Y.; Wang, Y. Tunable Electronic Structures of Hydrogenated Zigzag and Armchair Dumbbell Silicene Nanosheets: A Computational Study. *J. Phys. Chem. C* **2018**, *122*, 23208.

(14) Cahangirov, S.; Ongun¨ozçelik, V.; Ongun¨ozçelik, O.; Xian, L.; Avila, J.; Cho, S.; Asensio, M. C.; Ciraci, S.; Rubio, A. Atomic Structure of the $\sqrt{3} \times \sqrt{3}$ Phase of Silicene on Ag(111). *Phys. Rev. B* **2014**, *90*, 035448.

(15) Tang, P.; Chen, P.; Cao, W.; Huang, H.; Cahangirov, S.; Xian, L.; Xu, Y.; Zhang, S.-C.; Duan, W.; Rubio, A. Stable Two-Dimensional Dumbbell Stanene: A Quantum Spin Hall Insulator. *Phys. Rev. B* **2014**, *90*, 121408.

(16) Ongun, V. O.; Durgun, E.; Ciraci, S. New Phases of Germanene. *J. Phys. Chem. Lett* **2014**, *5*, 2694.

(17) Peng, X.; Wei, Q.; Copple, A. Strain-Engineered Direct-Indirect Band Gap Transition and Its Mechanism in Two-Dimensional Phosphorene. *Phys. Rev. B* **2014**, *90*, 085402.

(18) Ray, S. J.; Venkata Kamalakar, M. Unconventional Strain-Dependent Conductance Oscillations in Pristine Phosphorene. *Phys. Chem. Chem. Phys.* **2018**, *20*, 13508.

(19) Chaudhury, A.; Majumder, S.; Ray, S. J. Proximity-Induced Colossal Conductivity Modulation in Phosphorene. *Phys. Rev. Appl.* **2019**, *10*, 24056.

(20) Wu, Q.; Shen, L.; Yang, M.; Cai, Y.; Huang, Z.; Feng, Y. P. Electronic and Transport Properties of Phosphorene Nanoribbons. *Phys. Rev. B - Condens. Matter Mater. Phys.* **2015**, *92*, 035436.

(21) Carvalho, A.; Wang, M.; Zhu, X.; Rodin, A. S.; Su, H.; Castro Neto, A. H. Phosphorene: From Theory to Applications. *Nat. Rev. Mater.* **2016**, *1*, 16061.

(22) Zhou, W.; Guo, S.; Zhang, S.; Zhu, Z.; Yang, S. A.; Chen, M.; Cai, B.; Qu, H.; Zeng, H. Unusual Electronic Transitions in Two-Dimensional Layered SnSb2Te4 Driven by Electronic State Rehybridization. *Phys. Rev. Appl.* **2019**, *11*, 064045.

(23) Ray, S. J.; Venkata Kamalakar, M.; Chowdhury, R. Ab Initio Studies of Phoshorene Island Single Electron Transistor. *J. Phys. Condens. Matter* **2016**, *28*, 195302.

(24) Ray, S. J. First-Principles Study of MoS2, Phosphorene and Graphene Based Single Electron Transistor for Gas Sensing Applications. *Sensors Actuators B Chem.* **2016**, *222*, 492.

(25) Venkata Kamalakar, M.; Madhushankar, B. N.; Dankert, A.; Dash, S. P. Low Schottky Barrier Black Phosphorus Field-Effect Devices with Ferromagnetic Tunnel Contacts. *Small* **2015**, *11*, 2209–2216.

(26) Nair, A. et. al. Dramatic Magnetic Phase Designing in Phosphorene. *Phys. Chem. Chem. Phys.* **2019**, *21* (42), 23713–23719.

(27) Das, S.; Demarteau, M.; Roelofs, A. Ambipolar Phosphorene Field Effect Transistor. *ACS Nano* **2014**, *8* (11), 11730.

(28) Kamalakar, M. V.; Madhushankar, B. N.; Dankert, A.; Dash, S. P. Effect of High-k Dielectric and Ionic Liquid Gate on Nanolayer Black-Phosphorus Field Effect Transistors. *Appl. Phys. Lett.* **2015**, *107* (11), 113103.

(29) Kaur, S.; Kumar, A.; Srivastava, S.; Pandey, R.; Tankeshwar, K. Stability and Carrier Transport Properties of Phosphorene-Based Polymorphic Nanoribbons. *Nanotechnology* **2018**, *29*, 155701.

(30) Zhang, S.; Xie, M.; Li, F.; Yan, Z.; Li, Y.; Kan, E.; Liu, W.; Chen, Z.; Zeng, H. Semiconducting Group 15 Monolayers: A Broad Range of Band Gaps and High Carrier Mobilities. *Angew. Chemie - Int. Ed.* **2016**, *55*, 1666.

(31) Guo, S.; Zhang, Y.; Ge, Y.; Zhang, S.; Zeng, H.; Zhang, H. 2D V-V Binary Materials: Status and Challenges. *Adv. Mater.* **2019**, *31*, 1902352.

(32) Brent, J. R.; Savjani, N.; Lewis, E. A.; Haigh, S. J.; Lewis, D. J.; O'Brien, P. Production of Few-Layer Phosphorene by Liquid Exfoliation of Black Phosphorus. *Chem. Commun.* **2014**, *50*, 13338.

(33) Zeng, J.; Cui, P.; Zhang, Z. Half Layer By Half Layer Growth of a Blue Phosphorene Monolayer on a GaN (001) Substrate. *Phys. Rev. Lett.* **2017**, *118*, 046101.

(34) Zhao, T.; He, C. Y.; Ma, S. Y.; Zhang, K. W.; Peng, X. Y.; Xie, G. F.; Zhong, J. X. A New Phase of Phosphorus: The Missed Tricycle Type Red Phosphorene. *J. Phys. Condens. Matter* **2015**, *27*, 265301.

(35) Wu, M.; Fu, H.; Zhou, L.; Yao, K.; Zeng, X. C. Nine New Phosphorene Polymorphs with Non-Honeycomb Structures: A Much Extended Family. *Nano Lett.* **2015**, *15*, 3557.

(36) Wang, H.; Li, X.; Liu, Z.; Yang, J. ψ-Phosphorene: A New Allotrope of Phosphorene. *Phys. Chem. Chem. Phys.* **2017**, *19*, 2402.

(37) Li, P.; Luo, W. A New Structure of Two-Dimensional Allotropes of Group V Elements. *Sci. Rep.* **2016**, *6*, 25423.

(38) Xu, M.; He, C.; Zhang, C.; Tang, C.; Zhong, J. First-Principles Prediction of a Novel Hexagonal Phosphorene Allotrope. *Phys. Status Solidi - Rapid Res. Lett.* **2016**, *10*, 563.

(39) Perdew, J. P.; Burke, K.; Ernzerhof, M. Generalized Gradient Approximation Made Simple. *Phys. Rev. Lett.* **1996**, *77*, 3865.

(40) Soler, J. M.; Artacho, E.; Gale, J. D.; García, A.; Junquera, J.; Ordejón, P.; Sánchez-Portal, D. The SIESTA Method for Ab Initio Order-N Materials Simulation. *J. Phys. Condens. Matter* **2002**, *14*, 2745.

(41) Bradeen, J.; Shockley, W. Deformation Potentials and Mobilities in Non-Polar Crystals. *Phys. Rev.* **1950**, *80*, 72.

(42) Qiao, J.; Kong, X.; Hu, Z.-X.; Yang, F.; Ji, W. High-Mobility Transport Anisotropy and Linear Dichroism in Few-Layer Black Phosphorus. *Nat. Commun.* **2014**, *5*, 4475.

(43) Gaddemane, G.; Vandenberghe, W. G.; Van de Put, M. L.; Chen, S.; Tiwari, S.; Chen, E.; Fischetti, M. V. Theoretical Studies of Electronic Transport in Monolayer and Bilayer Phosphorene: A Critical Overview. *Phys. Rev. B* **2018**, *98*, 115416.

(44) Kresse, G.; Furthmüller, J. Efficient Iterative Schemes for Ab Initio Total-Energy Calculations Using a Plane-Wave Basis Set. *Phys. Rev. B - Condens. Matter Mater. Phys.* **1996**, *54*, 11169.

(45) Lee, C.; Kysar, J. W.; Hone, J. Measurement of the Elastic Properties and Intrinsic Strength of Monolayer Graphene Graphene Oxide View Project Nanomechanics View Project. *Science (80-.).* **2008**, *321*, 385.

(46) Lang, H.; Zhang, S.; Liu, Z. Mobility Anisotropy of Two-Dimensional Semiconductors. *Phys. Rev. B* **2016**, *94*, 235306.

(47) Tersoff, J.; Hamann, D. R. Theory and Application for the Scanning Tunneling Microscope. *Phys. Rev. B* **1985**, *31*, 805.

(48) Nigam, S.; Gupta, S.; Banyai, D.; Pandey, R.; Majumder, C. Evidence of a Graphene-like Sn-Sheet on a Au(111) Substrate: Electronic Structure and Transport Properties from First Principles Calculations. *Phys. Chem. Chem. Phys* **2015**, *17*, 6705.

(49) Kumar, A.; Banyai, D.; Ahluwalia, P. K.; Pandey, R.; Karna, S. P. Electronic Stability and Electron Transport Properties of Atomic Wires Anchored on the MoS 2 Monolayer. *Phys. Chem. Chem. Phys* **2014**, *16*, 20157.

(50) He, H.; Pandey, R.; Pati, R.; Karna, S. P. Spin-Polarized Electron Transport of a Self-Assembled Organic Monolayer on a Ni(111) Substrate: An Organic Spin Switch. *Phys. Rev. B* **2006**, *73*, 195311.

(51) Pati, R.; Senapati, L.; Ajayan, P. M.; Nayak, S. K. First-Principles Calculations of Spin-Polarized Electron Transport in a Molecular Wire: Molecular Spin Valve. *Phys. Rev. B* **2003**, *68*, 100407.

(52) Jamdagni, P.; Thakur, A.; Kumar, A.; Ahluwalia, P. K.; Pandey, R. Two Dimensional Allotropes of Arsenene with a Wide Range of High and Anisotropic Carrier Mobility. *Phys. Chem. Chem. Phys.* **2018**, *20*, 29939.

(53) Şahin, H.; Cahangirov, S.; Topsakal, M.; Bekaroglu, E.; Akturk, E.; Senger, R. T.; Ciraci, S. Monolayer Honeycomb Structures of Group-IV Elements and III-V Binary Compounds: First-Principles Calculations. *Phys. Rev. B* **2009**, *80*, 155453.

(54) Kamal, C.; Ezawa, M. Arsenene: Two-Dimensional Buckled and Puckered Honeycomb Arsenic Systems. *Phys. Rev. B* **2015**, *91*, 85423.

(55) Wang, J.; Zhang, M.; Meng, J.; Li, Q.; Yang, J. Single-and Few-Layer BiOI as Promising Photocatalysts for Solar Water Splitting. *RSC Adv.* **2017**, *7*, 244446.

(56) Zhang, J.; Zhou, P.; Liu, J.; Yu, J. New Understanding of the Difference of Photocatalytic Activity among Anatase, Rutile and Brookite TiO2. *Phys. Chem. Chem. Phys.* **2014**, *16*, 20382.

(57) Gupta, U.; Rao, C. N. R. Hydrogen Generation by Water Splitting Using MoS2 and Other Transition Metal Dichalcogenides. *Nano Energy* **2017**, *41*, 49.

(58) Feng, J.; Qian, X.; Huang, C.-W.; Li, J. Strain-Engineered Artificial Atom as a Broad-Spectrum Solar Energy Funnel. *Nat. Photonics* **2012**, *6*, 866.

(59) Sa, B.; Li, Y.-L.; Qi, J.; Ahuja, R.; Sun, Z. Strain Engineering for Phosphorene: The Potential Application as a Photocatalyst. *J. Phys. Chem. C* **2014**, *118*, 26560.

(60) Ge, X.; Sumboja, A.; Wuu, D.; An, T.; Li, B.; Goh, F. W. T.; Hor, T. S. A.; Zong, Y.;

Liu, Z. Oxygen Reduction in Alkaline Media: From Mechanisms to Recent Advances of Catalysts. *Acs Catal.* **2015**, *8*, 4643.